Elucidation of the Transport Properties of Calcium-Doped High Entropy Rare Earth Aluminates for Solid Oxide Fuel Cell Applications

Mohana V. Kante, L. Ajai R. Lakshmi Nilayam, Horst Hahn, Subramshu S. Bhattacharya, Matthias T. Elm,* Leonardo Velasco,* and Miriam Botros*

Solid oxide fuel cells (SOFCs) are paving the way to clean energy conversion, relying on efficient oxygen-ion conductors with high ionic conductivity coupled with a negligible electronic contribution. Doped rare earth aluminates are promising candidates for SOFC electrolytes due to their high ionic conductivity. However, they often suffer from p-type electronic conductivity at operating temperatures above 500 °C under oxidizing conditions caused by the incorporation of oxygen into the lattice. High entropy materials are a new class of materials conceptualized to be stable at higher temperatures due to their high configurational entropy. Introducing this concept to rare earth aluminates can be a promising approach to stabilize the lattice by shifting the stoichiometric point of the oxides to higher oxygen activities, and thereby, reducing the p-type electronic conductivity in the relevant oxygen partial pressure range. In this study, the high entropy oxide $(Gd,La,Nd,Pr,Sm)AlO_3$ is synthesized and doped with Ca. The Ca-doped $(Gd,La,Nd,Pr,Sm)AlO_3$ compounds exhibit a higher ionic conductivity than most of the corresponding Ca-doped rare earth aluminates accompanied by a reduction of the p-type electronic conductivity contribution typically observed under oxidizing conditions. In light of these findings, this study introduces high entropy aluminates as a promising candidate for SOFC electrolytes.

1. Introduction

Designing efficient electrolytes is crucial for the development of high-performing solid oxide fuel cells (SOFCs). Efficient electrolytes need to retain a high oxygen-ion conductivity combined with negligible electronic conductivities at different operating temperatures, as well as in a wide oxygen partial pressure range varying from oxidizing conditions at the cathode (1 bar to 10^{-5} bar of $p(O_2)$) to highly reducing conditions at the anode (10^{-10} to 10^{-18} bar of $p(O_2)$).[1] Using unstable electrolytes with a non-negligible electronic conductivity results in ohmic losses reducing the performance of the fuel cell.[1] Perovskite-structured $ReMO_3$ (Re: rare earth elements, M: Al, Ga, In, Sc) are promising candidates as electrolytes in SOFC applications.[2] Although $ReMO_3$ are insulators, doping with alkali earth metals or any stable 2+ cation results in the formation of oxygen vacancies, and

M. V. Kante, L. A. R. L. Nilayam, H. Hahn, M. Botros
Institute of Nanotechnology
Karlsruhe Institute of Technology
Kaiserstr. 12, 76131 Karlsruhe, Germany
E-mail: miriam.botros@kit.edu

L. A. R. L. Nilayam
Karlsruhe Nano Micro Facility (KNMFi)
Karlsruhe institute of Technology
76344 Eggenstein-Leopoldshafen, Germany

H. Hahn
Department of Chemical, Biological and Materials Engineering
The University of Oklahoma
100 E. Boyd St., Norman, OK 73019, USA

S. S. Bhattacharya
Department of Metallurgical and Materials Engineering
Indian Institute of Technology Madras
Chennai 600036, India

M. T. Elm
Center for Materials Research
Institute of Experimental Physics I, and Institute of Physical Chemistry
Justus-Liebig-Universität Gießen
35392 Gießen, Germany
E-mail: matthias.elm@phys.chemie.uni-giessen.de

L. Velasco
Direccion academica
Universidad Nacional de Colombia sede de La Paz
Km 9 via Valledupar – La Paz, Cesar 202010, Colombia
E-mail: lvelascoe@unal.edu.co

**ADVANCED
SCIENCE NEWS**

www.advancedsciencenews.com

NANO · MICRO

small

www.small-journal.com

thus, in a sufficiently high oxygen ion conductivity. $La_{1-x}Sr_xGa_{1-y}Mg_yO_{3-(x+y)/2}$ is the most commonly used perovskite-structured $ReMO_3$ for applications as electrolytes in SOFCs.[3] However, Ga is often substituted by Al to reduce the costs of the compounds and doped rare earth aluminates have been investigated as a cheaper alternative for $La_{1-x}Sr_xGa_{1-y}Mg_yO_{3-(x+y)/2}$. Several studies on doped rare earth aluminates suggest a dominant p-type conductivity under oxidizing conditions and a stable ionic conductivity at reducing conditions.[2,4–8] The dominant p-type conductivity in rare earth aluminates at high oxygen activity arises from the interaction between the crystal and the atmosphere. At high oxygen partial pressure, oxygen fills the oxygen vacancies and electron holes are created to ensure charge neutrality. This oxidation reaction is given in Kröger–Vink notation by

$$\frac{1}{2}O_2 + V_O^{\bullet\bullet} \leftrightarrow O_O^x + 2h^\bullet \tag{1}$$

where $V_O^{\bullet\bullet}$, O_O^x, and $h^\bullet$ denote the oxygen vacancy with a relative charge of +2, the oxygen ion on the oxygen lattice site, and the electron hole, respectively.

High-entropy materials are single-phase multicomponent materials with high configurational entropy (ΔS_{mix}). Conceptually, high entropy materials are assumed to have higher structural stability at high temperatures as the Gibbs free energy for formation $\Delta G = \Delta H - T\Delta S$ is reduced due to a high configurational entropy (ΔS_{mix}). This increases the overall entropy, which counterbalances the formation enthalpy. The high entropy concept was initially introduced in 2004 for alloys relevant to high-temperature applications.[9] Since then, a significant number of compositions of high entropy alloys have been studied confirming their improved structural stability and applicability at higher temperatures.[10–12] In 2015, the high entropy concept was introduced for oxides[13] followed by various investigations of their dielectric,[14] thermal,[15] electrochemical,[16] catalytic,[17] magnetic,[18] mechanical,[19] or ionic transport properties.[20] The studies were conducted for several compounds with a variety of different crystal structures, like Rocksalt,[13,19] fluorite,[20–22] perovskite,[15,23,24] spinel,[25–27] layered,[28] or pyrochlore[29] structure, to name a few. According to several reports, the thermal stability of several oxides could be improved by utilizing the high entropy concept including perovskite-type high entropy oxides.[13,24,31–33] Also doped high entropy rare earth aluminates might benefit from the increase of configurational entropy in order to thermally stabilize the crystals by pushing the oxidation reaction (Equation (1)) to the educt side, and thereby, decreasing the electronic conductivity in the system even under oxidating conditions and high operating temperatures (500–700 °C). In the present study, we introduced the high configurational entropy concept for rare earth aluminates as electrolytes for SOFCs. The samples are doped with Ca to increase the oxygen ion conductivity by generating oxygen vacancies $V_O^{\bullet\bullet}$. Using Kröger–Vink notation, the doping can be described by

$$CaO \xrightarrow{ReAlO_3} Ca_{Re}' + Al_{Al}^x + \frac{5}{2}O_O^\times + \frac{1}{2}V_O^{\bullet\bullet} \tag{2}$$
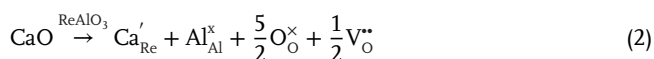
with Ca_{Re}' being a Ca^{2+} ion on a Re^{3+} lattice site with a relative charge of −1. The corresponding powders were synthesized us-
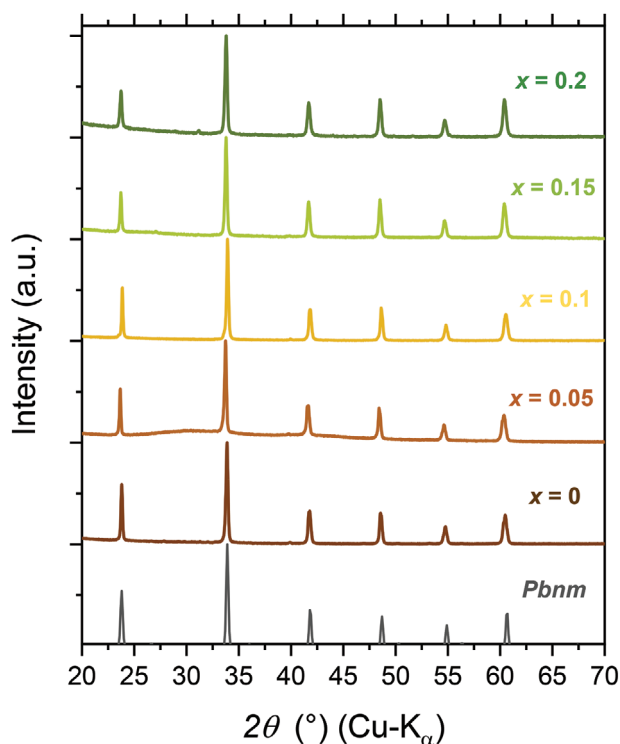
Figure 1. X-ray diffraction patterns of sintered pellets of $(Gd,La,Nd,Pr,Sm)_{1-x}Ca_xAlO_3$ ($x = 0$, 0.05, 0.1, 0.15, 0.2) with Asterix denoting the reflections of the secondary phase.

ing the Pechini process and consolidated into pellets via conventional sintering. X-ray diffraction (XRD), scanning electron microscopy (SEM), UV–vis spectroscopy, Raman spectroscopy, and transmission electron microscope (TEM) were conducted to characterize the high entropy oxides. The electrochemical properties were analyzed via electrochemical impedance spectroscopy (EIS) at different temperatures (300–700 °C) and for varying oxygen partial pressure (1 bar to 5 mbar). For comparison, also the Ca-doped single component rare earth aluminates ($Nd_{0.9}Ca_{0.1}AlO_3$, $Pr_{0.9}Ca_{0.1}AlO_3$, $Gd_{0.9}Ca_{0.1}AlO_3$, $Sm_{0.9}Ca_{0.1}AlO_3$ and $La_{0.9}Ca_{0.1}AlO_3$) were synthesized and characterized to elucidate the impact of increased configurational entropy on the transport properties of the Ca-doped high entropy aluminate.

2. Results and Discussion

2.1. Structural Characterization

Figure 1a shows the XRD patterns of the sintered $(Gd,La,Nd,Pr,Sm)_{1-x}Ca_xAlO_3$ pellets. $(Gd,La,Nd,Pr,Sm)AlO_3$, $(Gd,La,Nd,Pr,Sm)_{0.95}Ca_{0.05}AlO_3$, and $(Gd,La,Nd,Pr,Sm)_{0.9}Ca_{0.1}AlO_3$ exhibit a single phase with orthorhombic structure (space group of *Pbnm*) as further confirmed by Rietveld refinements presented in Figure S1, Supporting Information. For the $(Gd,La,Nd,Pr,Sm)_{0.85}Ca_{0.15}AlO_3$ and $(Gd,La,Nd,Pr,Sm)_{0.8}Ca_{0.2}AlO_3$ pellets, signatures of a minor secondary phase are observed. To identify the distortion from the ideal structure of a perovskite ABO_3,

**ADVANCED
SCIENCE NEWS**

www.advancedsciencenews.com

NANO · MICRO

small

www.small-journal.com

Table 1. Summary from Rietveld refinement, Williamson Hall plots, and relative density calculated from the Archimedes principle for $(Gd,La,Nd,Pr,Sm)_{1-x}Ca_xAlO_3$ pellets.

Composition	Tolerance factor	Crystallographic space group	Lattice parameter [Å]	Crystallite size [nm]	Relative density [%]
$(Gd,La,Nd,Pr,Sm)AlO_3$	0.968	*Pbnm*	$a = 5.29$	303	94
			$b = 5.32$		
			$c = 7.49$		
$(Gd,La,Nd,Pr,Sm)_{0.95}Ca_{0.05}AlO_3$	0.970	*Pbnm*	$a = 5.29$	323	96
			$b = 5.32$		
			$c = 7.49$		
$(Gd,La,Nd,Pr,Sm)_{0.9}Ca_{0.1}AlO_3$	0.972	*Pbnm*	$a = 5.29$	303	96
			$b = 5.31$		
			$c = 7.49$		
$(Gd,La,Nd,Pr,Sm)_{0.85}Ca_{0.15}AlO_3$	0.974	*Pbnm* unknown (<5%)	$a = 5.29$	308	92
			$b = 5.31$		
			$c = 7.50$		
$(Gd,La,Nd,Pr,Sm)_{0.8}Ca_{0.2}AlO_3$	0.976	*Pbnm* unknown (<5%)	$a = 5.30$	277	96
			$b = 5.31$		
			$c = 7.51$		

we calculated the Goldschmidt tolerance factor t of the prepared pellets[30]

$$t = \frac{r_A + r_O}{\sqrt{2}\,(r_B + r_O)} \tag{3}$$

where r_A is the effective A-site cationic radii, r_O is ionic radii of oxygen, and r_B is ionic radii of the cation on B-site. For an ideal cubic perovskite holds $t = 1$. If $t < 1$, the crystals exhibit an orthorhombic or rhombohedral structure. The calculated tolerance factors of the different $(Gd,La,Nd,Pr,Sm)_{1-x}Ca_xAlO_3$ pellets with varying x are listed in **Table 1**. The ionic radii are taken from the ionic radii database of the Atomistic Simulation Group of the Materials Department of Imperial College.[31,32] All prepared systems show a tolerance factor of less than 1, suggesting an orthorhombic structure. The ionic radius of the Ca ion is similar to that of rare earth cations. Thus, only small changes in the lattice parameters are observed with increasing Ca content. The relative densities of the $(Gd,La,Nd,Pr,Sm)_{1-x}Ca_xAlO_3$ pellets determined using Archimedes principle are also listed in Table 1. The XRD patterns of the Ca-doped single component rare earth oxides ($Gd_{0.9}Ca_{0.1}AlO_3$, $La_{0.9}Ca_{0.1}AlO_3$, $Nd_{0.9}Ca_{0.1}AlO_3$, $Pr_{0.9}Ca_{0.1}AlO_3$, and $Sm_{0.9}Ca_{0.1}AlO_3$) can be seen in the Figure S2, Supporting Information. All Ca-doped single-component systems exhibit a single-phase orthorhombic structure synonymous with that of the high entropy aluminates. The structure and relative densities of the Ca-doped single component oxides are also shown in Table S1, Supporting Information.

2.2. Microstructural and Chemical Characterization

Representative SEM micrographs showing inside the pores found at the surface of the pellets are displayed in **Figure 2**. The SEM micrographs show highly densified pellets and large grains with diameters in the micrometer range, that is, significant grain growth occurs during the long sintering time at high tempera-

tures. All Ca-doped samples exhibit a comparable grain size. Only for the undoped counterpart, the grain size is slightly larger. SEM low magnification images of the polished surfaces can be found in Figure S3, Supporting Information.

Along with the microstructural characterization, we studied the chemical composition of the pellets using energy-dispersive X-ray spectroscopy (EDX). The percentage of cations on the A-site is shown in **Figure 3**. For all compositions, we observe that the pellets have near-stoichiometric values of Gd, La, Nd, Pr, Sm, and Ca. Only the amounts of La and Pr are slightly higher or lower, respectively, compared to the stoichiometric value.

Transmission electron microscopy (TEM) was conducted on the powder sample of $(Gd,La,Nd,Pr,Sm)_{0.9}Ca_{0.1}AlO_3$ (**Figure 4**a). The selected area electron diffraction (SAED) pattern shown in Figure 4b further confirms the crystallinity of the sample. Elemental maps from EDX spectra presented in Figure 4d–i reveal that the elements are distributed homogeneously with no visible segregation on the nanoscale. The corresponding elemental quantification of the maps can be seen in Figure S4, Supporting Information.

2.3. Raman Spectroscopy

Figure 5 shows the Raman spectra of the $(Gd,La,Nd,Pr,Sm)_{1-x}Ca_xAlO_3$ pellets prepared. The Raman band of the undoped compound at around 241 cm^{-1} corresponds to the internal vibration A_g mode vibration of ReO_9 dodecahedra.[33,34] Adding Ca into $(Gd,La,Nd,Pr,Sm)AlO_3$ results in new bands appearing at around 514, 608, and 687 cm^{-1}, which are attributed to the B_{1g}, B_{2g}, and B_{3g} vibrational modes of the BO_6 octahedra in the $CaBO_3$ system.[35,36] The appearance of additional Raman bands further confirms the successful incorporation of Ca into the crystal structure. No major change in the position of the Raman modes is observed with the addition of Ca. As the Raman spectrum of material reflects the crystal symmetry of the material, it is evident that all $(Gd,La,Nd,Pr,Sm)_{1-x}Ca_xAlO_3$ pellets exhibit the same crystal
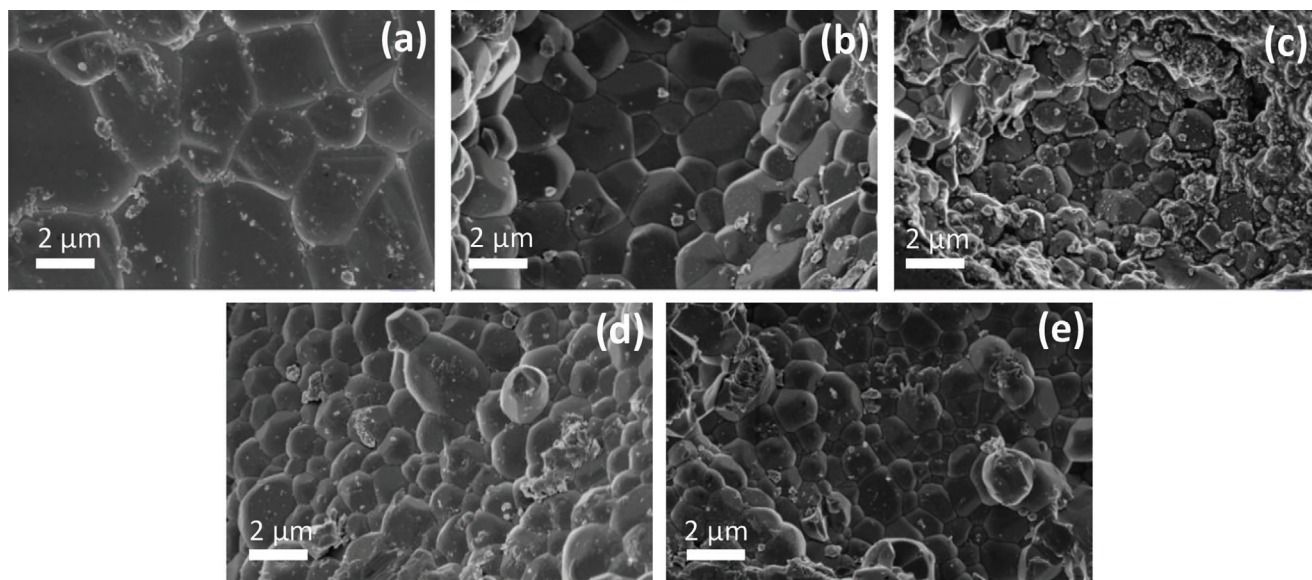
Figure 2. SEM micrographs showing inside the pores encountered at the surface of $(Gd,La,Nd,Pr,Sm)_{1-x}Ca_xAlO_3$ with a) $x = 0$, b) $x = 0.05$, c) $x = 0.1$, d) $x = 0.15$, and e) $x = 0.2$.

symmetry in agreement with the XRD data shown in Figure 1 and Table 1.

2.4. UV–Vis Spectroscopy

The optical band gap of the pellets was determined from the absorbance α measured by UV–Vis spectroscopy. The corresponding spectra are shown in Figure S5, Supporting Information. Determining the optical band gap can provide valuable information about the oxidation state of Pr in the rare earth oxides. Pr is well known to exhibit multivalency (+3, +4) depending on the system and experimental conditions. A change in the oxidation state of Pr changes the optical band gap of Pr containing rare earth oxides.[37–39] Consequently, the band gaps of rare earth aluminates provide insights into the electronic states of Pr ion. Direct band gaps are considered for rare earth aluminates according to various reports.[40–43] Thus, $(\alpha h\nu)^{\frac{1}{2}}$ is plotted versus the photon energy $h\nu$ (Tauc plot) as shown in **Figure 6**a. The incorporation of Ca into $(Gd,La,Nd,Pr,Sm)AlO_3$ results in a strong shift of the absorbance edge to lower energies, while the absorbance at higher energies shows two maxima at about 4 and 5.2 eV independent of the doping content. The optical band gaps of the $(Gd,La,Nd,Pr,Sm)_{1-x}Ca_xAlO_3$ pellets are determined from the extrapolation of the absorbance edge to zero using a linear fit. As shown in Figure 6b, the optical band gap drastically decreases with the addition of Ca to $(Gd,La,Nd,Pr,Sm)AlO_3$. The lowest band gap is observed for $x = 0.05$, which increases again with increasing Ca content. The strong decrease of the optical band gap indicates a change in the Pr oxidation state, that is, the doping with Ca does not necessarily create oxygen vacancies according to Equation (2). If Pr is present in the compound, the Ca incorporation can also be compensated by the formation of a hole

$$CaO \xrightarrow{ReAlO_3} Ca'_{Re} + Al^x_{Al} + \frac{5}{2}O^\times_O + h^\bullet \qquad (4)$$
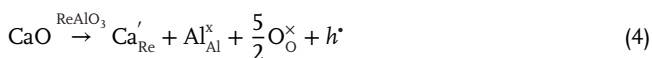
which, then, localizes on the Pr site forming a small polaron, that is, the Pr oxidation state changes from +III to +IV

$$Pr^x_{Pr} + h^\bullet \rightarrow Pr^\bullet_{Pr} \qquad (5)$$

where Pr^x_{Pr} and $Pr^\bullet_{Pr}$ denotes the Pr^{3+} and Pr^{4+} ion, respectively. The change of the Pr oxidation state has a significant impact on the optical absorption in oxides.[37–39] As shown by Szubka et al. for $LaAlO_3$,[44] the occupied O 2p states and the unoccupied La 5d states form the valence and the conduction band, respectively, while the occupied 4f and 4s states of Pr^{3+} are located inside the band gap. A comparable situation is found for Pr-doped ceria, where the oxygen 2p states and the empty cerium d states form the valence and conduction band.[45] The occupied Pr^{3+} and Ce^{3+} states are located inside the band gap and significantly affect the optical properties.[45–47] Thus, it is reasonable to assume that also the 4f states of the Pr^{+3} are involved in the formation of the conduction band in the case of $(Gd,La,Nd,Pr,Sm)AlO_3$. Consequently, the optical absorption in $(Gd,La,Nd,Pr,Sm)AlO_3$ arises from the excitation of electrons from the occupied Pr^{3+} states located inside the band gap into the empty conduction band as schematically depicted in Figure 6c. If Pr^{4+} is formed according to reaction R4, empty Pr^{4+} states are present inside the band gap and optical absorption from the valence band to the Pr^{4+} states can already occur at lower excitation energies. At higher energies, excitation from the Pr^{3+} states to the conduction band still occurs, which is reflected by the comparable absorbance of all samples for $h\nu \geq 4$ eV.

2.5. Electrochemical Measurements

The electrical properties of the $(Gd,La,Nd,Pr,Sm)_{1-x}Ca_xAlO_3$ pellets were characterized using EIS, which was performed at different temperatures and under varying oxygen partial
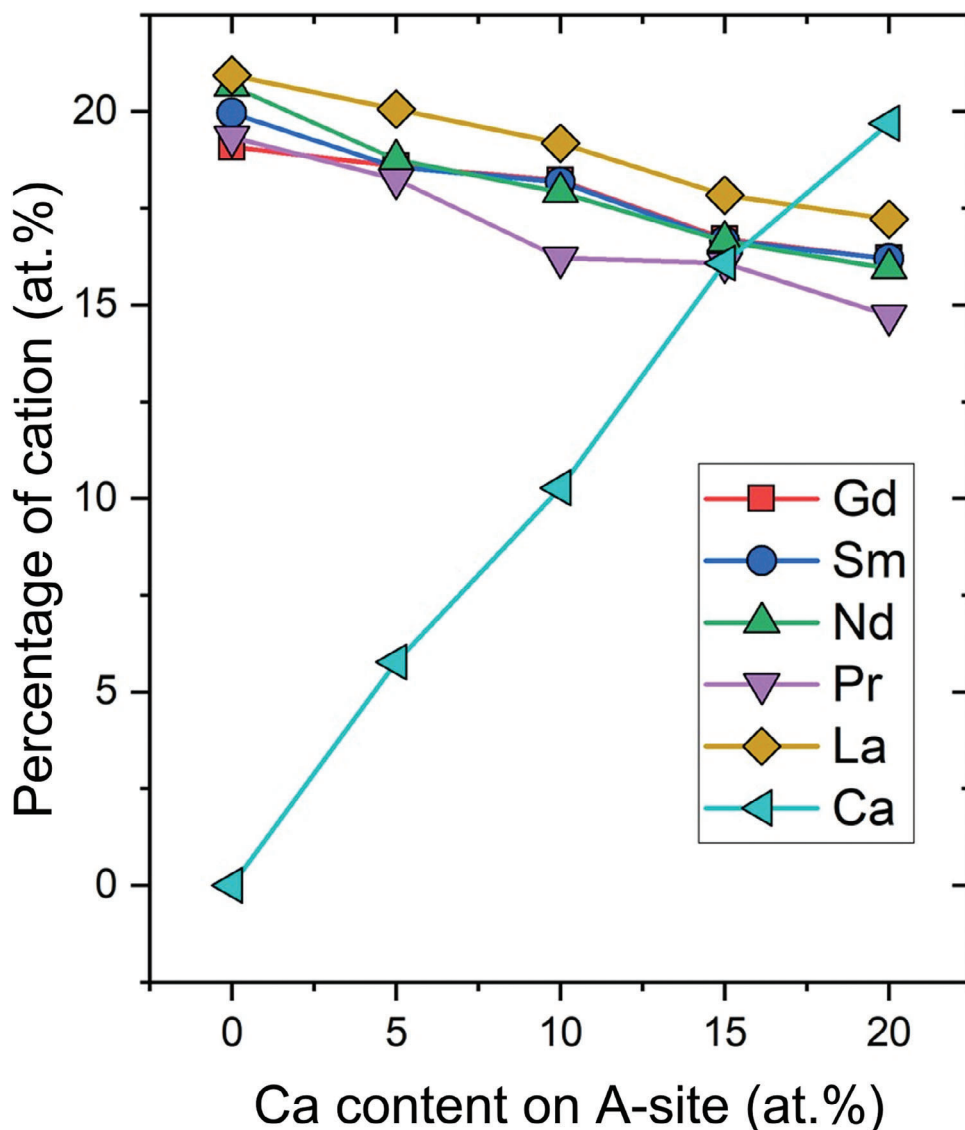
**Figure 3.** Percentage of cations on A site (± 0.2%) of $(Gd,La,Nd,Pr,Sm)_{1-x}Ca_xAlO_3$ determined using SEM-EDX.

pressure $(-2.5 < \log(p(O_2)/bar) <)$. The Nyquist plots showing the impedance spectra of $(Gd,La,Nd,Pr,Sm)_{0.9}Ca_{0.1}AlO_3$ measured at 350 and 600 °C in the ambient atmosphere $(\log(p(O_2)/bar) = -0.7)$ is displayed in **Figure 7**. The Nyquist representation of the spectra changes from three full semicircles at 350 °C (a) to an arc with a small high-frequency semicircle at 600 °C. The three semicircles at 350 °C can be attributed to contributions from the grains (high-frequency range), the grain boundaries (intermediate frequency range), and the electrode (low-frequency range). Each contribution is described by an *RQ* element, where *R* is the resistance of the transport process and *Q* is a constant phase element (CPE) accounting for the non-ideal capacitive response. The impedance is fitted by an equivalent circuit consisting of the three *RQ* elements connected in series as shown in the inset of Figure 7. With increasing tem-

perature, the characteristic frequencies of the different processes shift to higher frequency values due to a decrease in the resistance $(\tau = \frac{2\pi}{\omega} = RC)$ and, thus, only the grain boundaries and the electrode are visible in the impedance spectrum at 600 °C. Consequently, only two *RQ* elements are considered in the corresponding equivalent circuit at higher temperatures (Figure 7b). The CPE and resistance values obtained from the fit are listed in Table S2, Supporting Information. From the parameters of the CPE elements, the capacitance of the processes can be calculated. The obtained capacitance values are characteristic of the corresponding transport processes, confirming the suitability of the equivalent circuit.[48,49]

As grain and grain boundary contribution can only be separated at low temperatures, only the total resistance, that is, the sum of grain and grain boundary resistance, can be obtained in
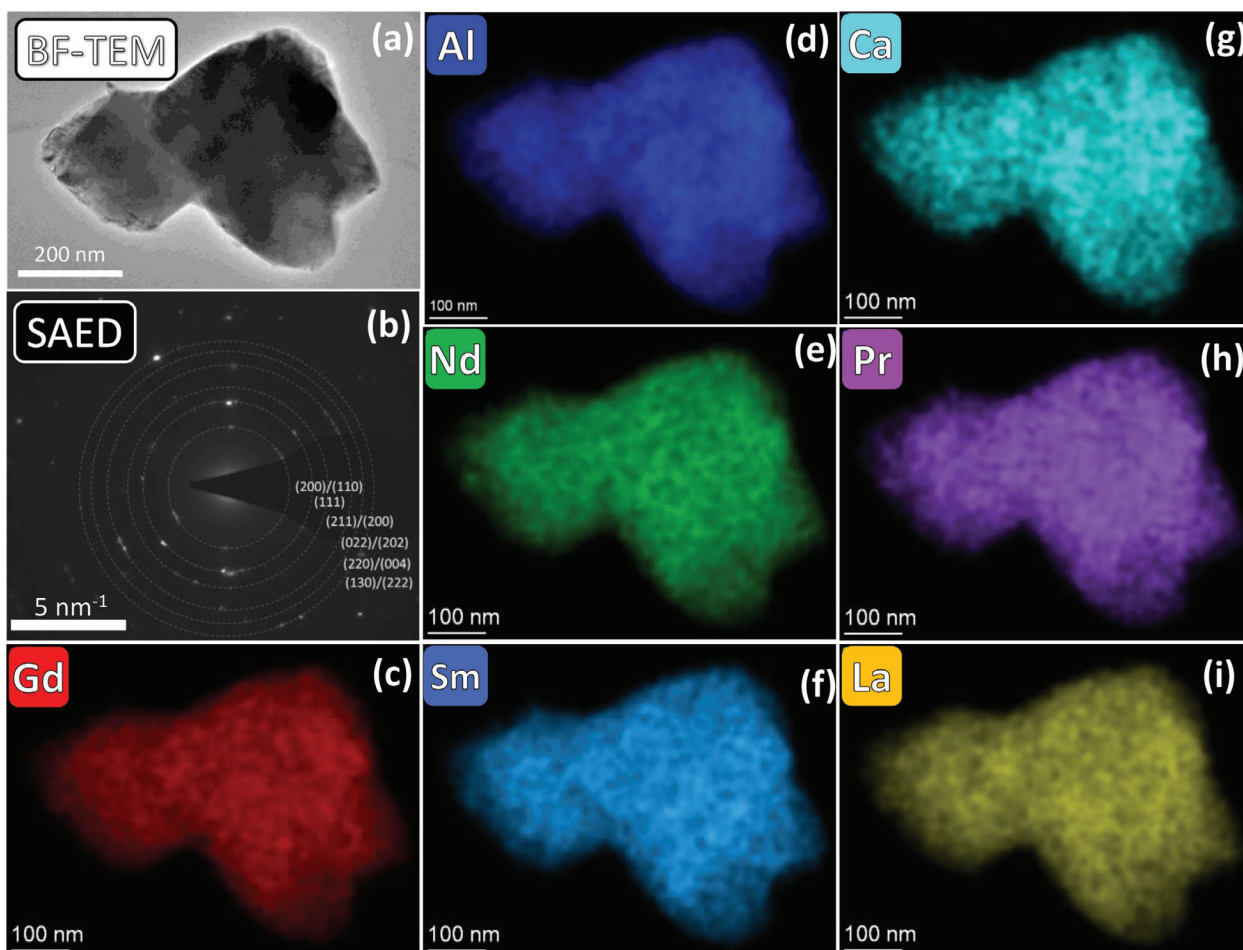
Figure 4. a) High-angle annular dark-field transmission electron micrograph and b) selected area electron diffraction of a $(Gd,La,Nd,Pr,Sm)_{0.9}Ca_{0.1}AlO_3$ particle. c–i) Element maps for Gd, Al, Nd, Sm, Ca, Pr, La of the corresponding particle. EDX data had been treated with Gaussian blur to improve the quality of the data. The corresponding quantification can be seen in Figure S4, Supporting Information.

the whole temperature range investigated. From the total resistance, the conductivity of the pellets is calculated

$$\sigma = \frac{1}{R} \frac{l}{A} \tag{6}$$

where l and A denote the thickness and the cross-sectional area, respectively, of the pellets. **Figure 8a** shows the temperature-dependence of the total conductivity (grain and grain boundary contribution) of the differently doped $(Gd,La,Nd,Pr,Sm)_{1-x}Ca_xAlO_3$ pellets in an Arrhenius representation. The conductivity of $(Gd,La,Nd,Pr,Sm)AlO_3$ shows a non-linear temperature dependence in the Arrhenius representation with a change in slope at around 627 and 827 °C, which is probably due to a phase transition from the orthorhombic to a rhombohedral structure.[50–52] In contrast, the Ca-doped counterparts exhibit an almost linear temperature dependence, which allows the determination of the activation energies E_A of the Ca-doped pellets

$$\sigma_{tot}(T) = \frac{\sigma_0}{T} \exp\left(-\frac{E_A}{k_B T}\right) \tag{7}$$

The obtained E_A values range from ≈0.89 to 1.01 eV and are shown in Figure 8. However, a closer look reveals a kink in the slope of the conductivity ≈500 °C. This indicates a change in the dominant transport mechanism.[2,5] More importantly, the total conductivity increases by nearly four orders of magnitude due to Ca-doping as the introduction of Ca on rare earth cation sites increases the number of oxygen vacancies $V_O^{\bullet\bullet}$ due to charge neutrality reasons, and thus, increases the oxygen ion conductivity of the material as described in Equation (8). Although the ionic conductivity is expected to be directly related to the concentration of oxygen vacancies, that is

$$\sigma_{ion}(T) = 2e\mu_{ion}(T)\left[V_O^{\bullet\bullet}\right] \tag{8}$$

it is nearly independent of the Ca content in the $(Gd,La,Nd,Pr,Sm)_{1-x}Ca_xAlO_3$ samples and even slightly decreases for high Ca content as shown in Figure 8b. This is due to a decrease in ion mobility μ_{ion} at high doping concentrations caused by defect interactions and/or the formation of defect associates, for example, oxygen vacancies trapped at the Ca dopants.[1,4,52–55] Typically, a maximum in oxygen ion conductivity is achieved for doping concentrations between 5%

**ADVANCED
SCIENCE NEWS**
www.advancedsciencenews.com

NANO · MICRO
small
www.small-journal.com
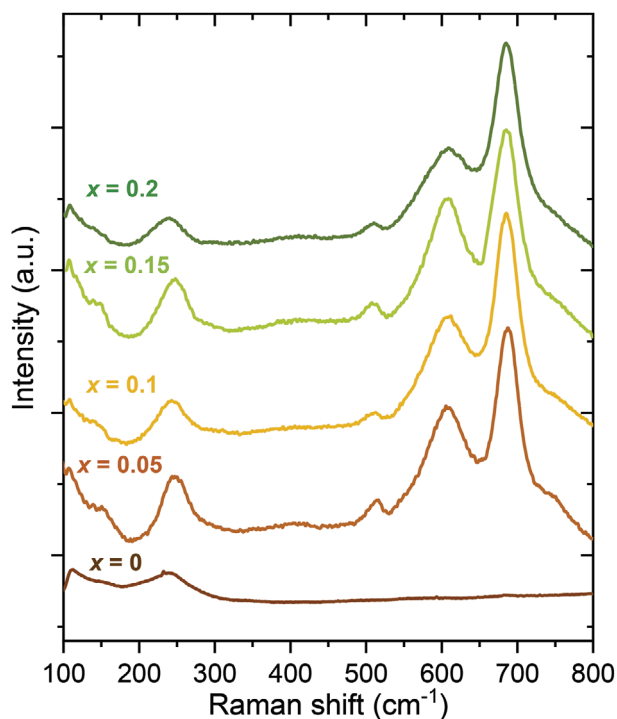
Figure 5. Raman spectra of $(Gd,La,Nd,Pr,Sm)_{1-x}Ca_xAlO_3$ with $x = 0$, 0.05, 0.1, 0.15, and 0.2.

and 10% in agreement with the results observed in this study. Figure 8c shows the oxygen-partial pressure dependence of the total conductivity in the range from 0.005 to 1 bar at different temperatures. A constant conductivity is observed at 400 and 500 °C confirming a dominant ionic conductivity due to the Ca-doping as expected according to Equation (8). However, the conductivity increases with increasing $p(O_2)$ in the high partial pressure range for temperatures above 500 °C, which reveals an additional p-type electron conductivity contribution as often observed for various aluminate oxides.[2,4,5] The presence of a mixed ionic-electronic conductivity behavior at temperatures above 500 °C can also be related to the change in activation energy as discussed above.

2.6. Comparison with Doped Single Component Rare Earth Aluminates

The conductivity behavior of the high entropy aluminate $(Gd,La,Nd,Pr,Sm)_{0.9}Ca_{0.1}AlO_3$ is compared with the individual Ca-doped single component rare earth aluminates $(La_{0.9}Ca_{0.1}AlO_3$, $Pr_{0.9}Ca_{0.1}AlO_3$, $Nd_{0.9}Ca_{0.1}AlO_3$, $Sm_{0.9}Ca_{0.1}AlO_3$, and $Gd_{0.9}Ca_{0.1}AlO_3)$, which are synthesized with the same synthesis route. The temperature dependence and the $p(O_2)$-dependence of the conductivities are presented in **Figure 9**. The $Pr_{0.9}Ca_{0.1}AlO_3$ sample exhibits a significantly higher conductivity than the HEO $(Gd,La,Nd,Pr,Sm)_{0.9}Ca_{0.1}AlO_3$. The conductivities of all other Ca-doped single-component rare earth aluminates are lower, in particular at low temperatures, and vary as follows: $\sigma_{LaCaAlO_3} > \sigma_{NdCaAlO_3} > \sigma_{SmCaAlO_3} > \sigma_{GdCaAlO_3}$ as seen in Figure 9.

The magnitude of the conductivities follows a similar trend as the ionic radii of the rare earth cation with $r_{La} > r_{Nd} > r_{Sm} > r_{Gd}$. Thus, the results show that a decrease in the ionic radius of the rare earth cation, that is, the decrease of the Goldschmidt tolerance factor, increases the distortion in the lattice, which blocks the pathway of the oxygen ions. Consequently, the conductivity also decreases with decreasing radius of the rare earth cation in the Ca-doped rare earth aluminates. The obstruction of oxygen ion diffusion and decrease in conductivity due to different cation sizes has been well explored in various oxygen ion conductors.[1–3,56] As for the HEO, the temperature-dependence of the total conductivity of all aluminates in Arrhenius representation exhibits a kink at 500 °C suggesting a transition in nature of the conductivity above 500 °C (Figure 9). In order to clarify the underlying transport mechanism, the $p(O_2)$-dependence of the conductivity is investigated in the range of oxidizing atmospheres (1 bar to 5 mbar). As shown in **Figure 10**a–f, all samples exhibit an increase in conductivity with increasing $p(O_2)$ at temperatures above 500 °C. Similar trends are well reported in literature.[2,4,6–8,57,58]

The $p(O_2)$-dependence of the conductivity can be derived considering the oxidation reaction (Equation (1)). The corresponding equilibrium constant is given by
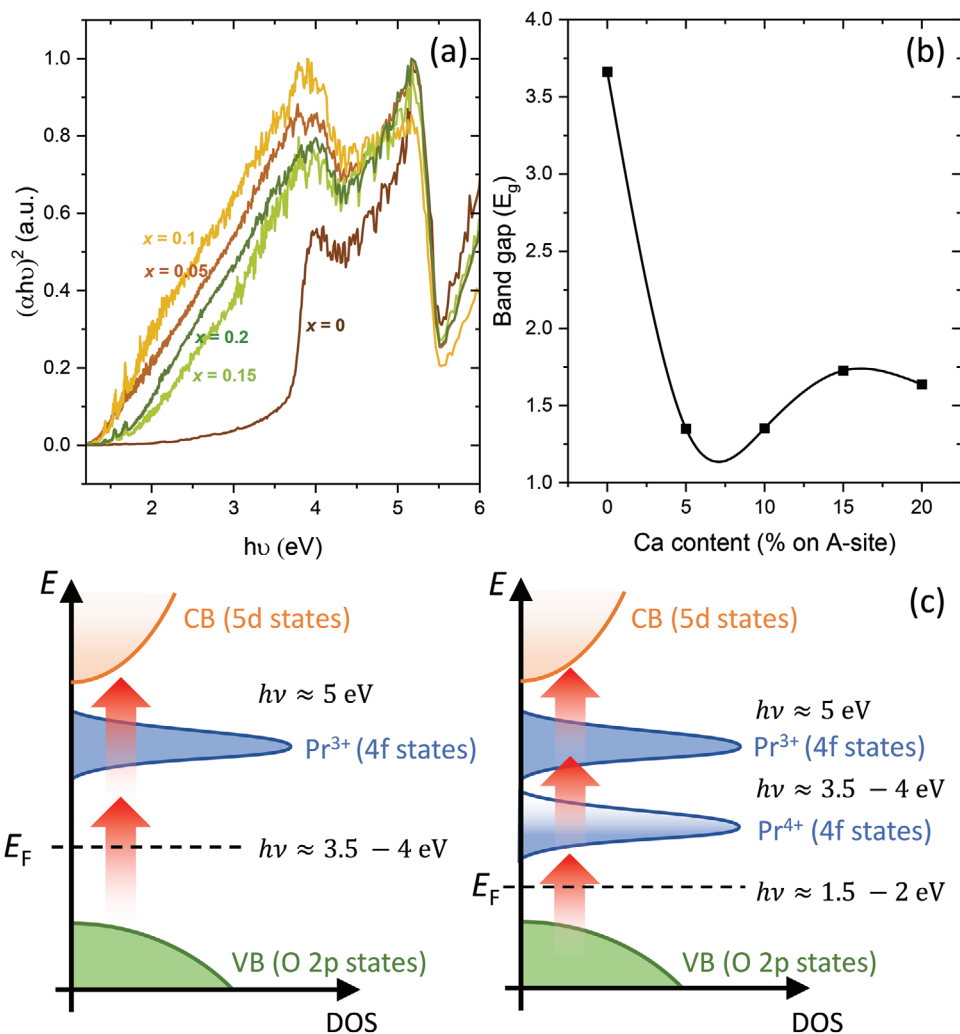
$$K_{ox} = \frac{[V_O^{\bullet\bullet}]\, p(O_2)^{\frac{1}{2}}}{[O_o^x]\,[h^{\bullet}]^2} \tag{9}$$

Due to the Ca-doping, the vacancy concentration in the samples can be assumed to be constant, that is, $2\,[V_O^{\bullet\bullet}] = [Ca'_{Re}]$ (Brouwer approximation). For the $p(O_2)$-dependence of the hole concentration and thus, the p-type electronic conductivity contribution due to small polarons, follows Equation (10)[2]

$$\sigma_{pol} \propto [h^{\bullet}] = \sqrt{\frac{[V_O^{\bullet\bullet}]}{[O_o^x]\,K_{ox}}}\, p(O_2)^{\frac{1}{4}} \tag{10}$$

A comparison reveals that the increase of the conductivity for $La_{0.9}Ca_{0.1}AlO_3$ (Figure 10a), $Nd_{0.9}Ca_{0.1}AlO_3$ (Figure 10b), $Pr_{0.9}Ca_{0.1}AlO_3$ (Figure 10e) follows the expected $p(O_2)^{\frac{1}{4}}$-dependence revealing a dominant p-type conductivity contribution. For the other samples, the $p(O_2)^{\frac{1}{4}}$-dependence is less pronounced. Also with decreasing temperature, the hole conductivity decreases and the conductivities remain unchanged with varying $p(O_2)$ except for $Pr_{0.9}Ca_{0.1}AlO_3$. In particular, the $Gd_{0.9}Ca_{0.1}AlO_3$ (Figure 10d) sample exhibit an almost constant conductivity over the whole partial pressure range at 400 °C. This indicates that the ionic conductivity contribution dominates at this temperature and low oxygen partial pressure, that is, all samples except for $Pr_{0.9}Ca_{0.1}AlO_3$ exhibit a mixed ionic electronic conductivity. In addition, the results reveal that the high total conductivity of $Pr_{0.9}Ca_{0.1}AlO_3$ arises solely from a high p-type electronic conductivity contribution.
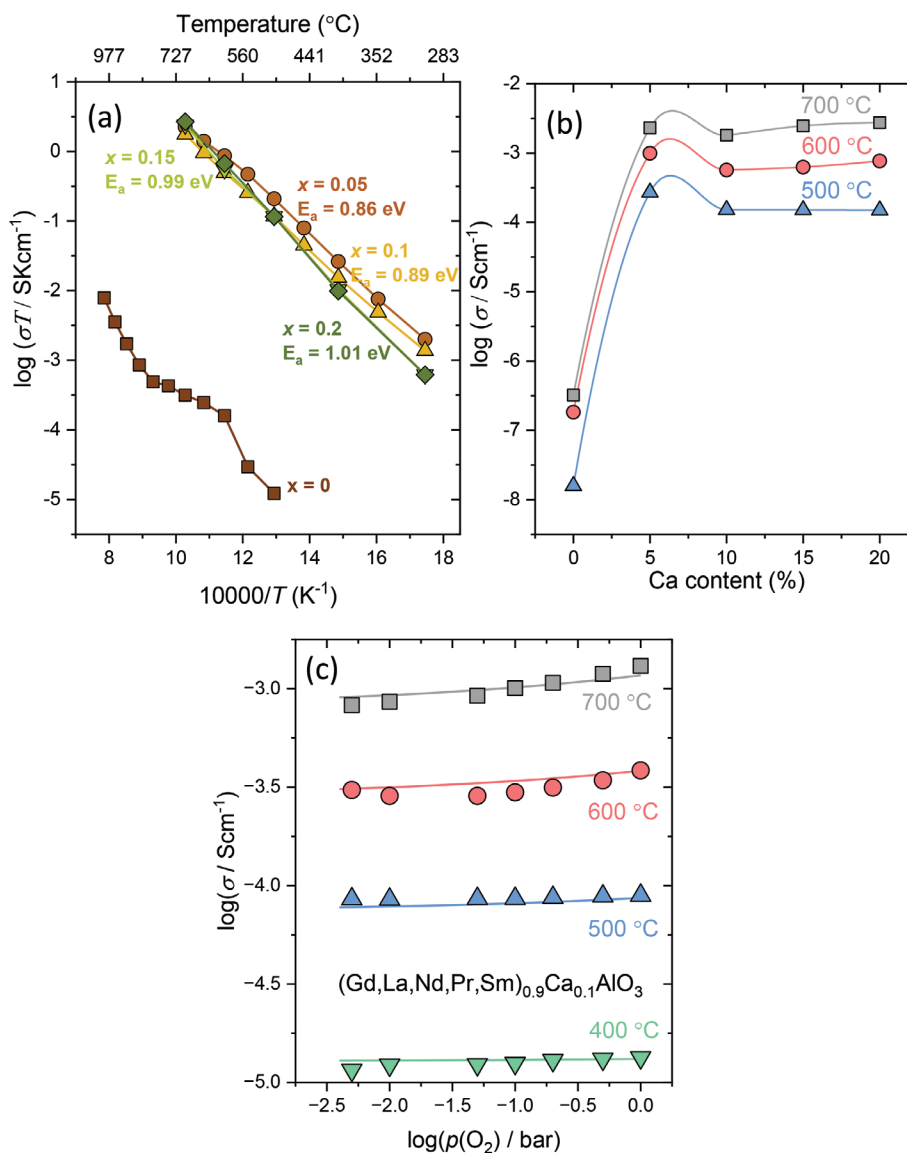
Due to the high Pr content in the sample, the incorporation of Ca is partly compensated by the formation of holes forming small polarons as described in Equations (3) and (4). In

**ADVANCED
SCIENCE NEWS**

www.advancedsciencenews.com

NANO · MICRO

small

www.small-journal.com

Figure 6. a) Tauc plot of the absorbance of the $(Gd,La,Nd,Pr,Sm)_{1-x}Ca_xAlO_3$ pellets derived from the UV–vis spectra shown in Figure S3, Supporting Information. b) Direct band gap of pellets of $(Gd,La,Nd,Pr,Sm)_{1-x}Ca_xAlO_3$. c) Simple depiction of valence orbitals of rare earth oxides.
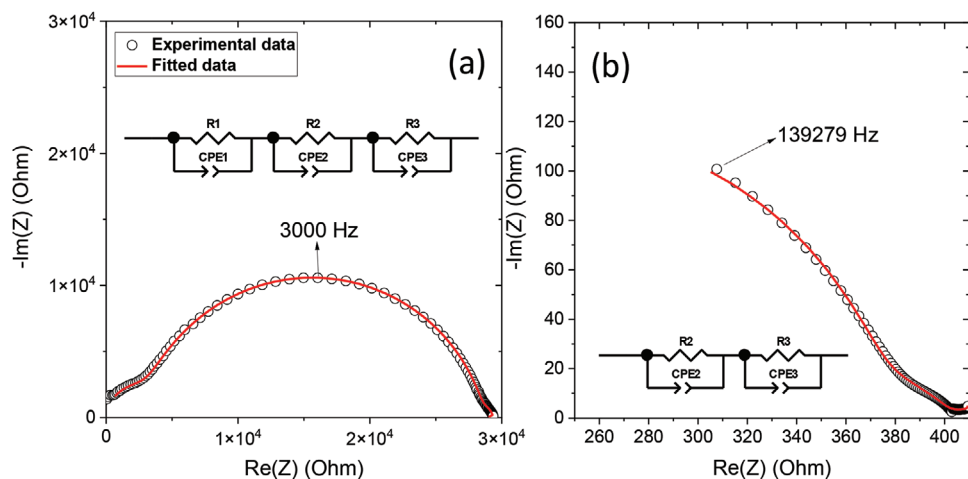
Figure 7. Nyquist plots, corresponding equivalent circuit of $(Gd,La,Nd,Pr,Sm)_{0.9}Ca_{0.1}AlO_3$ at a) 350 °C and b) 600 °C. The fit to the impedance data using the equivalent circuit is shown as a solid line.
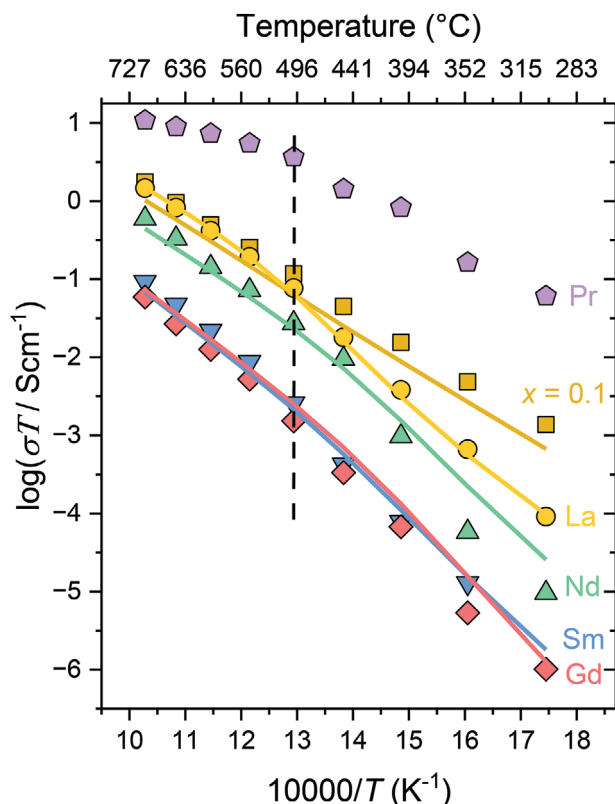
**ADVANCED
SCIENCE NEWS**

www.advancedsciencenews.com

NANO · MICRO

small

www.small-journal.com

Figure 8. a) Arrhenius plots of $(Gd,La,Nd,Pr,Sm)_{1-x}Ca_xAlO_3$ ($x = 0, 0.05, 0.1, 0.15, 0.2$), b) variation of conductivity with change in Ca content at different temperatures. c) Change in conductivity of $(Gd,La,Nd,Pr,Sm)_{0.9}Ca_{0.1}AlO_3$ with partial pressure of oxygen from 0.005 to 1 bar. Fits of the conductivity using Equations (12), (13), and (16) are shown as solid lines.

addition, it is well reported that Pr easily changes its oxidation state in the $p(O_2)$ range investigated.[39,59,60] The presence of a relatively higher Pr^{4+} content in $Pr_{0.9}Ca_{0.1}AlO_3$ is also confirmed by electron energy loss spectroscopy (EELS) (**Figure 11a**). Pr exhibits two energy loss peaks (M_5 and M_4) around 920 and 960 eV, which arise from transitions from the 4f to the 3d orbitals. The intensity ratio between the M_5 and M_4 peaks (I_{M5}/I_{M4}) is a suitable value to compare the oxidation states of Pr.[61,62] The higher the I_{M5}/I_{M4} ratio, the lower is the Pr^{4+} concentration.[62] The I_{M5}/I_{M4} values obtained confirm that Pr^{+4} is the minority charge carrier, that is, hole transport dominates in the samples. They also reveal that the Pr^{+4} concentration is higher in $Pr_{0.9}Ca_{0.1}AlO_3$ than in the HEO-$(Gd,La,Nd,Pr,Sm)_{0.9}Ca_{0.1}AlO_3$. The higher Pr content in $Pr_{0.9}Ca_{0.1}AlO_3$ also affects the mobility μ_{pol} of the small polarons, which strongly depend on the available Pr^{3+} lattice sites. The p-

type electronic conductivity σ_{pol} due to small polarons is given by[59,63]

$$\sigma_{pol} = e[h^\bullet] \, \mu_{pol} = e \left[Pr_{Re} \right] x_{Pr}^{4+} \left(1 - x_{Pr}^{4+} \right) \frac{\mu_{pol}^0}{T}$$

$$\times \exp \left(-\frac{\Delta H_{mig}}{k_B T} \right) p \left(O_2 \right)^{\frac{1}{4}}$$

$$= \frac{\sigma_{pol,0}}{T} \exp \left(-\frac{E_A}{k_B T} \right) p(O_2)^{\frac{1}{4}} \qquad (11)$$

where e is the elementary charge, μ_{pol} is the polaron mobility, $\sigma_{pol,0}$ is the polaron conductivity pre-factor, $E_A = \Delta H_{mig}$ is the migration enthalpy for the hopping process, and $[h^\bullet]$ is the

**ADVANCED
SCIENCE NEWS**

www.advancedsciencenews.com

NANO · MICRO
small

www.small-journal.com

Figure 9. Comparison of Arrhenius plots of (Gd,La,Nd,Pr, Sm)$_{0.9}$Ca$_{0.1}$AlO$_3$ (HEO) with doped single component aluminates (La$_{0.9}$Ca$_{0.1}$AlO$_3$ (La), Pr$_{0.9}$Ca$_{0.1}$AlO$_3$ (Pr), Nd$_{0.9}$Ca$_{0.1}$AlO$_3$ (Nd), Sm$_{0.9}$Ca$_{0.1}$AlO$_3$ (Sm), Gd$_{0.9}$Ca$_{0.1}$AlO$_3$ (Gd)). The symbols are the experimental data along with solid lines which are fits derived from Equations (12), (13), and (16).

concentration of holes, which can hop as small polarons through the lattice. The latter is strongly dependent on the probability of finding a pathway for the polaron to hop from Pr^{+4} to an adjacent Pr^{+3}, which is reflected by the expression [Pr$_{Re}$] $x_{Pr}^{4+}(1 - x_{Pr}^{4+})$ with [Pr$_{Re}$] being the concentration of Pr ions in the compound. Figure 11b shows a typical orthorhombic perovskite. The unit cell of the orthorhombic structure can be divided into two small cubes with A-sites at the center, B-sites at the corners, and 8 oxygen-ions at the edge centers. The number of A-sites adjacent to an A-site is given by the 6 planes of the A-site centered cube in Figure 11b. In Pr$_{0.9}$Ca$_{0.1}$AlO$_3$, a Pr ion is surrounded by at least 6 Pr ions and the number of Pr^{+4} in the adjacent 6 ions can be estimated to be around 1–2 assuming 10% Pr^{+4}. This provides at least one possible pathway for small polaron propagation from Pr^{4+} to Pr^{3+}. However, in (Gd,La,Nd,Pr,Sm)$_{0.9}$Ca$_{0.1}$AlO$_3$, the number of Pr ions surrounding an adjacent Pr ion reduces from 6 to only 1. Consequently, the possibility of finding a Pr^{+4} adjacent to Pr^{+3} becomes much lower, which restricts the mobility of the small polarons. The increased number of possible hopping sites combined with a higher concentration of small polarons (Pr^{4+}) explains the significantly higher total conductivity of Pr$_{0.9}$Ca$_{0.1}$AlO$_3$.

As the Pr$_{0.9}$Ca$_{0.1}$AlO$_3$ sample shows no ionic plateau, that is, no mixed ionic-electronic conductivity, it is not further explored in this study. However, a detailed analysis of the temperature- and

oxygen partial pressure-dependence of the total conductivity of all other compounds allows the estimation of the p-type electronic and ionic contribution to the total conductivity. The total conductivity is given as the sum of both contributions

$$\sigma_{tot}\left(T, p\left(O_2\right)\right) = \sigma_{ion}\left(T\right) + \sigma_{pol}\left(T, p\left(O_2\right)\right) \quad (12)$$

Following Equation (8), the temperature-dependence of the ionic conductivity can be written as

$$\sigma_{ion}\left(T\right) = 2e\left[V_O^{\bullet\bullet}\right]\frac{\mu_{ion}^0}{T}\exp\left(-\frac{\Delta H_{ion}}{k_B T}\right) = \frac{\sigma_{ion,0}}{T}\exp\left(-\frac{E_A^{ion}}{k_B T}\right) \quad (13)$$

where $\Delta H_{ion} = E_A^{ion}$ denotes the migration enthalpy for the oxygen ions. The p-type electronic conductivity due to polarons dominates in the high $p(O_2)$-range, where a kink in the temperature-dependence of the total conductivity is observed. Thus, two different transport processes with different activation energies contribute to σ_{pol} at low and high temperatures, respectively. The kink in the temperature dependence might be due to the presence of grain boundaries in the samples (cf. Figure 2). It is well reported that grain boundaries in oxides are characterized by a space-charge region,[65–67] which may affect the activation energy for the hopping process of the polarons. It is also possible that the kink arises from holes, which are trapped at dopants or impurities forming associates[68] such as

$$Ca_{Re}' + h^{\bullet} \leftrightarrow \left(Ca_{Re}' h^{\bullet}\right)^{x} \quad (14)$$
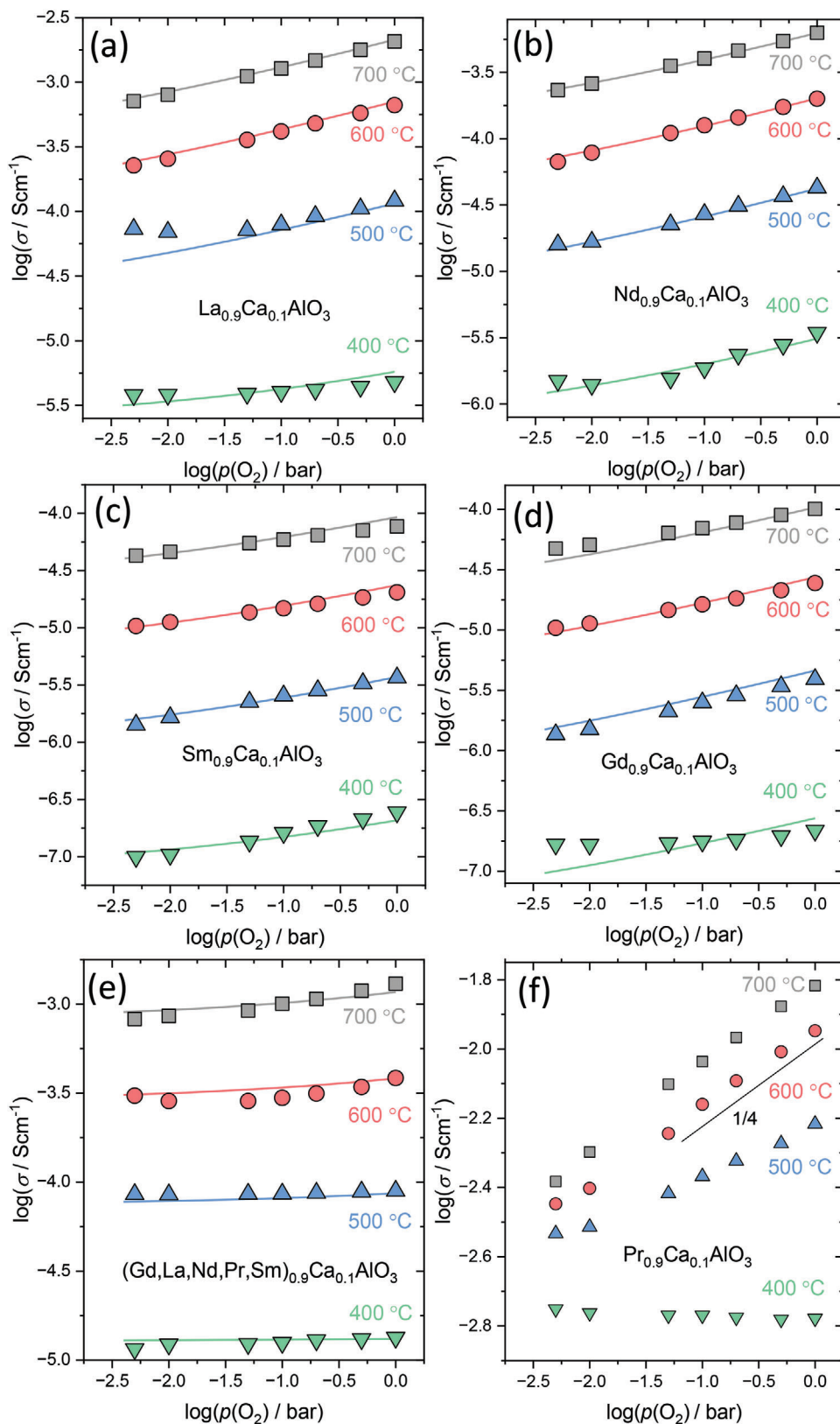
The different activation energy at low temperatures, then, comprises the binding energy of the associate. A comparable situation is found, for example, in yttria-stabilized zirconia or La$_{1-x}$Sr$_x$Ga$_{1-y}$Mg$_y$O$_{3-(x+y)/2}$, where oxygen vacancies are trapped at the dopants.[69–71] However, in both cases the resistances of the two transport processes add up and, thus, the p-type conductivity is described by[72]

$$\sigma_{pol}\left(T, p\left(O_2\right)\right) = \left(\frac{1}{\sigma_{pol}^{LT}} + \frac{1}{\sigma_{pol}^{HT}}\right)^{-1} = \frac{\sigma_{pol}^{LT}\sigma_{pol}^{HT}}{\sigma_{pol}^{LT} + \sigma_{pol}^{HT}} \quad (15)$$

The temperature- and $p(O_2)$-dependence of each polaronic process can also be described by Equation (11). Thus, for the p-type conductivity follows

$$\sigma_{pol}\left(T, p\left(O_2\right)\right)$$
$$= \frac{\sigma_{pol,0}^{LT}\sigma_{pol,0}^{HT}}{T}\left(\frac{\exp\left(-\frac{E_A^{LT}+E_A^{HT}}{k_B T}\right)}{\sigma_{pol,0}^{LT}\exp\left(-\frac{E_A^{LT}}{k_B T}\right) + \sigma_{pol,0}^{HT}\exp\left(-\frac{E_A^{HT}}{k_B T}\right)}\right)p\left(O_2\right)^{\frac{1}{4}} \quad (16)$$

with σ_{pol}^{LT}, σ_{pol}^{HT} and E_A^{LT}, E_A^{HT} being the polaron conductivity prefactor and the activation energy of the low- and high-temperature transport process, respectively. By combining Equations (12), (13), and (16), the total conductivity of each sample can be fitted in the whole temperature and $p(O_2)$-range investigated. For the fitting it is assumed that the three conductivity pre-factors

ADVANCED
SCIENCE NEWS

www.advancedsciencenews.com

NANO · MICRO

small

www.small-journal.com

Figure 10. Dependence of conductivities at different p(O₂) of a) $La_{0.9}Ca_{0.1}AlO_3$, b) $Nd_{0.9}Ca_{0.1}AlO_3$, c) $Sm_{0.9}Ca_{0.1}AlO_3$, d) $Gd_{0.9}Ca_{0.1}AlO_3$, e) $Pr_{0.9}Ca_{0.1}AlO_3$, and f) $(Gd,La,Nd,Pr,Sm)_{0.9}Ca_{0.1}AlO_3$ at different temperatures 400, 500, 600, and 700 °C. In the graph, symbols are the experimental data and solid lines are the fits obtained using Equations (12), (13), and (16).
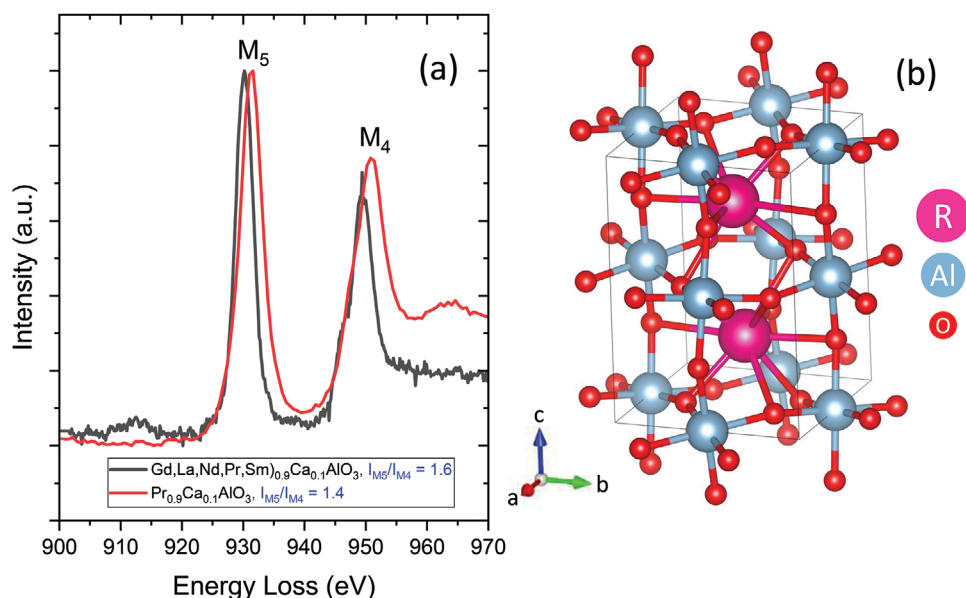
Figure 11. a) EELS data and I_{M5}/I_{M4} values of powders of $(Gd,La,Nd,Pr,Sm)_{0.9}Ca_{0.1}AlO_3$, $Pr_{0.9}Ca_{0.1}AlO_3$. The I_{M5}/I_{M4} values were derived from the integrated intensity of respective edges over a 5-eV range using a double-step background model (double arc tangent method). The EELS is deconvoluted using the Fourier ratio method. Both procedures were performed using the Digital Micrograph software also known as Gatan Microscopy Suite.[64] b) Lattice of an orthorhombic perovskite structure where R = La, Sm, Pr, Gd, Nd, and Ca.

$(\sigma_{ion,0}$, σ_{pol}^{LT}, $\sigma_{pol}^{HT})$ of all samples exhibit a comparable value independent of the composition of the rare earth metals. This is reasonable as the conductivity pre-factor is mainly determined by the concentration of mobile charge carriers, which is fixed by the Ca-doping (cf. Equations (2) and (10)). In addition, all samples exhibit the same crystal structure, that is, differences in the mobility pre-factor can be neglected in the first approxi-

mation. The ionic and polaron conductivity pre-factors obtained from the fitting are listed in Table S3, Supporting Information. The fits obtained are shown in Figures 8c, 9, and 10 as solid lines, while Figure S6, Supporting information, shows the different contributions of the three transport processes to the total conductivity of $La_{0.9}Ca_{0.1}AlO_3$. The activation energies obtained from the fitting procedure are compared in **Figure 12**. The activation
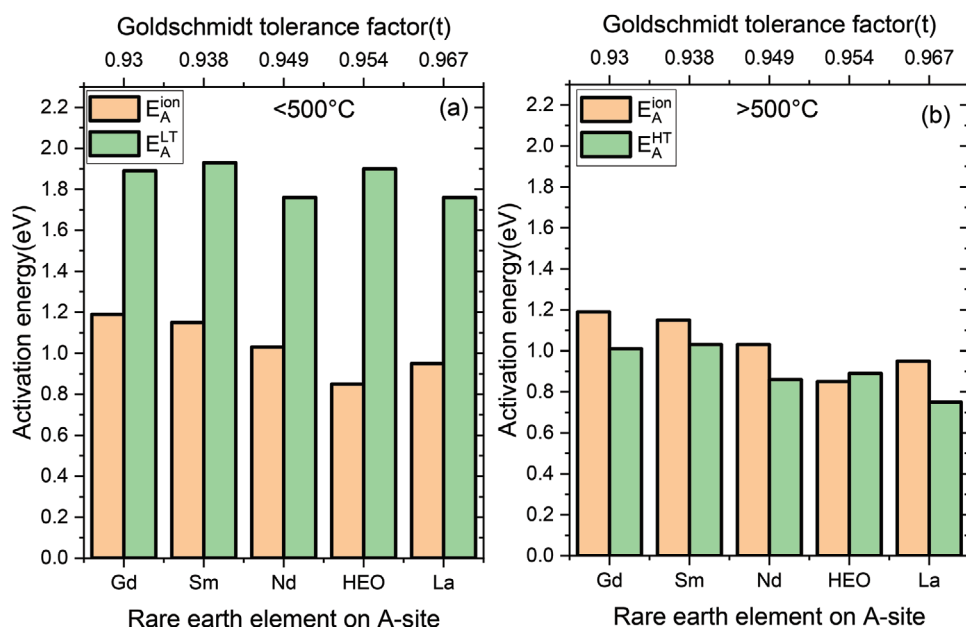
Figure 12. Comparison of the activation energy of the a) low-temperature and b) high-temperature electronic transport process with the activation energy of the ions plotted versus the tolerance factor (t) of $(Gd,La,Nd,Pr,Sm)_{0.9}Ca_{0.1}AlO_3$ -HEO, $La_{0.9}Ca_{0.1}AlO_3$ – La, $Nd_{0.9}Ca_{0.1}AlO_3$ – Nd, $Sm_{0.9}Ca_{0.1}AlO_3$ – Sm, $Gd_{0.9}Ca_{0.1}AlO_3$ – Gd.

**ADVANCED
SCIENCE NEWS**

www.advancedsciencenews.com

NANO · MICRO

small

www.small-journal.com

energies of the low-temperature polaronic transport process, E_A^{LT}, are higher than the activation energies E_A^{ion} for oxygen vacancy migration (Figure 12a). This is consistent with the dominant ionic conductivity below 500 °C. However, at temperatures above 500 °C, the activation energies of the high-temperature polaronic transport process, E_A^{HT}, are lower than E_A^{ion}, which explains the p-type electronic conductivity at higher temperatures. Only the HEO $(Gd,La,Nd,Pr,Sm)_{0.9}Ca_{0.1}AlO_3$ exhibits a E_A^{HT}, which is higher than the activation energies E_A^{ion} for oxygen ion migration, which explains the more dominant ionic conduction above 500 °C. On closer inspection, E_A^{HT} of the HEO represents an average of the E_A^{HT} of the corresponding rare earth aluminates. In addition, Figure 12 clearly shows that the activation energies of the doped single-component rare earth aluminates increase with decreasing tolerance factor, that is, the distortion of the lattice restricts the motion of the oxygen ions. This correlation between lattice distortion and mobility is very well explored in the literature.[1–3,56] However, the high entropy oxide does not follow this trend showing the lowest activation energy E_A^{ion}, although the tolerance factor is smaller than for the $La_{0.9}Ca_{0.1}AlO_3$ sample. This is consistent with the results of Hayashi et al., who found an optimal tolerance factor for high oxygen ion conductivity of $t = 0.96$ for ABO_3-based perovskites[73] and explains, why the HEO shows the highest ionic conductivity of all perovskites investigated. The approach of exploring the compositional space of high entropy materials successfully led to a unique composition with the lowest E_A^{ion} due to an optimum tolerance factor (0.96) accompanied with a relatively high E_A^{HT} owing to the synergy among the constituent rare earth elements. Furthermore, the conductivity of the HEO is compared to the conductivity of yttria-stabilized zirconia, which is the state-of-the-art electrolyte material for SOFCs. For this purpose, $Y_{0.08}Zr_{0.92}O_2$ (YSZ) pellets are consolidated and sintered from commercially available powders of $Y_{0.08}Zr_{0.92}O_2$ (Nelco). The SEM micrograph of the YSZ pellets can be seen in Figure S7, Supporting Information. The grain sizes of the YSZ and HEO are comparable. As a result, the contribution of grain boundary to the conductivity can be reasonably compared. As shown in **Figure 13**, the ionic conductivity of the HEO is slightly lower than that of YSZ at higher temperatures and comparable in the investigated low-temperature range. Thus, the results show that HEO are promising candidates as solid electrolytes for SOFC applications, in particular, as the ionic conductivity may be further enhanced by simultaneous doping of the A- and the B-site.[2,74]

3. Conclusion

High entropy materials are well known for their high-temperature stability and are potential candidates for high-temperature applications. In this work, the high entropy aluminate $(Gd,La,Nd,Pr,Sm)AlO_3$ is successfully synthesized and Ca is used as a dopant to enable oxygen ion conductivity in the compound making it a potential candidate as an electrolyte for SOFCs. Structural characterization using XRD and Raman confirms a phase pure orthorhombic perovskite structure (*Pbnm*) is observed and maintained upon Ca-doping up to 10%, while for a Ca content of 15% and 20% a secondary phase appears. Chemical characterization from EDX via TEM and SEM confirms the chemical stoichiometry and homogenous distribution of ele-
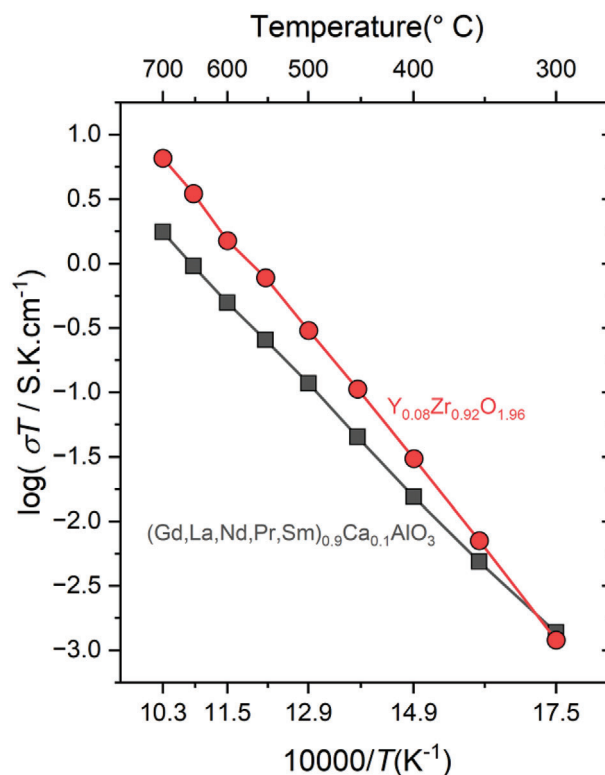

Figure 13. Arrhenius plot comparing the ionic conductivities of HEO and yttria-stabilized zirconia.

ments in the powder form. EELS and UV–Vis suggest the presence of small amounts of Pr^{+4} along with Pr^{+3}. Temperature- and oxygen partial pressure-dependent EIS measurements reveal an increased ionic conductivity compared to the Ca-doped rare earth aluminates $La_{0.9}Ca_{0.1}AlO_3$, $Nd_{0.9}Ca_{0.1}AlO_3$, $Sm_{0.9}Ca_{0.1}AlO_3$, and $Gd_{0.9}Ca_{0.1}AlO_3$, which is caused by a reduced ionic activation energy due to a restriction of the lattice distortion. Additionally, the activation energy for small polaron migration is relatively higher than the ionic activation energy, which suppresses the parasitic p-type electronic conductivity of the HEO under oxidizing conditions. Thus, the high entropy approach is successfully applied to rare earth aluminates for applications as electrolytes in SOFCs. The results demonstrate the suitability of the high entropy approach for designing advanced materials with enhanced thermal stability and tailored electrical properties for high-temperature applications.

4. Experimental Section

The high entropy aluminates $(Ga_{0.2}La_{0.2}Nd_{0.2}Pr_{0.2}Sm_{0.2})_{1−x}Ca_xAlO_3$ with $x = 0$, 0.05, 0.1, 0.15, and 0.2 and $Re_{0.9}Ca_{0.1}AlO_3$ (Re = Gd,La,Nd,Pr,Sm) powders were synthesized using a Pechini process. $Gd(NO_3)_3.6H_2O$ (Alfa Aesar, 99.9%), $La(NO_3)_3.6H_2O$ (Thermo Scientific, 99.9%), $Nd(NO_3)_3.6H_2O$ (Alfa Aesar, 99.9%), $Pr(NO_3)_3.6H_2O$ (Thermo Scientific,99.9%), $Sm(NO_3)_3.6H_2O$ (Sigma-Aldrich, 99.9%), $Ca(NO_3)_2.4H_2O$ (Fluka Analytical, > 99%), and $Al(NO_3)_3.9H_2O$ (VWR, > 99%) were mixed in water along with citric acid (Sigma Aldrich, > 99.5%, chelating agent) and ethylene glycol (Alfa Aesar, 99%, polymerizing agent). The ratio between metal ions, citric acid, and ethylene glycol was kept

constant at 1:1:2. The resulting solution was stirred at 140 °C for 1 h, dried at 300 °C, and then annealed at 1250 °C for 2 h to obtain the oxide powders. Subsequently, the powders were pressed into pellets at a pressure of 500 MPa and heat-treated at 1500 °C for 12 h resulting in densification.

The relative density (%) of the pellets was measured according to the Archimedes principle. XRD was conducted with a Bruker D8 advance Cu X-ray powder diffractometer equipped with a super speed detector. The XRD scans were measured over a 2θ range of 10–90° with a step size of 0.02° and a scan time of 3 and 5 s per step. Rietveld refinement was done using the FullProf software suite. The data were fitted using a Thompson-Cox-Hastings pseudo-Voigt axial divergence asymmetry peak model. Instrumental parameters, lattice parameters, atomic positions, and peak widths were fitted during the refinement. The instrumental parameters were derived from the XRD of standard LaB_6 and the Williamson Hall method was used to calculate the crystallite size. SEM was conducted in a Gemini Leo 1530 scanning electron microscope. SEM imaging was performed at an operating voltage and working distance of 5 kV and 5 mm, respectively. EDX was conducted inside the SEM with an X-Max^N Oxford instruments X-ray detector. EDX was performed at an operating voltage and distance of 20 kV and 8.5 mm, respectively. TEM, scanning transmission electron microscopy (STEM) micrographs, SAED patterns, EDX, and EELS data were acquired using a double aberration-corrected state-of-the art ThermoFischer Themis Z HR-(S)TEM equipped with a Super-X energy dispersive X-ray detector and a Gatan GIF Continuum 970 HighRes + K3 IS camera (operated at 300 kV). Raman spectra were collected using a Reinshaw in-via confocal microscope with a green laser (532 nm) at 100× magnification for 30 s and 10 accumulations. UV–Vis spectroscopy was conducted in an Agilent Cary 60 device with a remote fiber optic accessory. The scan was performed from 1100 to 200 nm with a speed of 600 nm min^{-1} in Reflectance mode. The absorbance was derived from the reflectance using the Kubelka–Munk function. Band gaps were determined from a Tauc plot analysis. For the electrochemical characterization, EIS silver paste was applied on both sides of the pellet and fired at 750 °C for 2 h to ensure good electrical contacts. The measurements were performed using a Bio-Logic VSP potentiostat. The temperature ranged from 350 to 700 °C. EIS measurements at different oxygen partial pressures were conducted by creating a vacuum with a Leopold Trivac vacuum pump and feeding in oxygen until the desired partial pressure was reached. The measurements were performed in a frequency range between 1 and 100 MHz with an amplitude of 500 mV.

Supporting Information

Supporting Information is available from the Wiley Online Library or from the author.

Acknowledgements

Conflict of Interest

The authors declare no conflict of interest.

Data Availability Statement

The data that support the findings of this study are available from the corresponding author upon reasonable request.

[1] S. C. Singhal, K. Kendall, *High-temperature Solid Oxide Fuel Cells: Fundamentals, Design and Applications*, Elsevier, New York **2003**.

[2] D. Lybye, F. W. Poulsen, M. Mogensen, *Solid State Ionics* **2000**, *128*, 91.

[3] S. J. Skinner, J. A. Kilner, *Mater. Today* **2003**, *6*, 30.

[4] T. L. Nguyen, M. Dokiya, S. Wang, H. Tagawa, T. Hashimoto, *Solid State Ionics* **2000**, *130*, 229.

[5] J. Y. Park, G. M. Choi, *Solid State Ionics* **2002**, *535*, 154.

[6] M. Fabián, B. I. Arias-Serrano, A. A. Yaremchenko, H. Kolev, M. Kaňuchová, J. Briančin, *J. Eur. Ceram. Soc.* **2019**, *39*, 5298.

[7] A. Sinha, H. Näfe, B. P Sharma, P. Gopalan, *J. Electrochem. Soc.* **2008**, *155*, B309.

[8] T. Tsuji, Y. Ohashi, Y. Yamamura, *Solid State Ionics* **2002**, *154–155*, 541.

[9] J. W. Yeh, S. K. Chen, S. J. Lin, J. Y. Gan, T. S. Chin, T. T. Shun, C. H. Tsau, S. Y. Chang, *Adv. Eng. Mater.* **2004**, *6*, 299.

[10] S. K. Dewangan, A. Mangish, S. Kumar, A. Sharma, B. Ahn, V. Kumar, *Eng. Sci. Technol., Int. J.* **2022**, *35*, 101211.

[11] S. Praveen, H. S. Kim, *Adv. Eng. Mater.* **2018**, *20*, 1700645.

[12] J. Chen, X. Zhou, W. Wang, B. Liu, Y. Lv, W. Yang, D. Xu, Y. Liu, *J. Alloys Compd.* **2018**, *760*, 15.

[13] C. M. Rost, E. Sachet, T. Borman, A. Moballegh, E. C. Dickey, D. Hou, J. L. Jones, S. Curtarolo, J. P. Maria, *Nat. Commun.* **2015**, *6*, 8485.

[14] D. Bérardan, S. Franger, D. Dragoe, A. K. Meena, N. Dragoe, *Phys. Status Solidi RRL* **2016**, *10*, 328.

[15] T. Maiti, R. Banerjee, S. Chatterjee, M. Ranjan, T. Bhattacharya, S. Mukherjee, S. S. Jana, A. Dwivedi, *ACS Sustainable Chem. Eng.* **2020**, *8*, 17022.

[16] A. Sarkar, L. Velasco, D. Wang, Q. Wang, G. Talasila, L. de Biasi, C. Kübel, T. Brezesinski, S. S. Bhattacharya, H. Hahn, B. Breitung, *Nat. Commun.* **2018**, *9*, 3400.

[17] S. H. Albedwawi, A. AlJaberi, G. N. Haidemenopoulos, K. Polychronopoulou, *Mater. Des.* **2021**, *202*, 109534.

[18] A. Sarkar, R. Kruk, H. Hahn, *Dalton Trans.* **2021**, *50*, 1973.

[19] W. Hong, F. Chen, Q. Shen, Y. H. Han, W. G. Fahrenholtz, L. Zhang, *J. Am. Ceram. Soc.* **2019**, *102*, 2228.

[20] K. Chen, X. Pei, L. Tang, H. Cheng, Z. Li, C. Li, X. Zhang, L. An, *J. Eur. Ceram. Soc.* **2018**, *38*, 4161.

[21] R. Djenadic, A. Sarkar, O. Clemens, C. Loho, M. Botros, V. S. K. Chakravadhanula, C. Kübel, S. S. Bhattacharya, A. S. Gandhi, H. Hahn, *Mater. Res. Lett.* **2017**, *5*, 102.

[22] H. Xu, Z. Zhang, J. Liu, C. L. Do-Thanh, H. Chen, S. Xu, Q. Lin, Y. Jiao, J. Wang, Y. Wang, Y. Chen, S. Dai, *Nat. Commun.* **2020**, *11*, 3908.

[23] A. Sarkar, R. Djenadic, D. Wang, C. Hein, R. Kautenburger, O. Clemens, H. Hahn, *J. Eur. Ceram. Soc.* **2018**, *38*, 2318.

[24] S. Jiang, T. Hu, J. Gild, N. Zhou, J. Nie, M. Qin, T. Harrington, K. Vecchio, J. Luo, J. Luo, *Scr. Mater.* **2017**, *142*, 116.

ADVANCED
SCIENCE NEWS

www.advancedsciencenews.com

NANO · MICRO
small

www.small-journal.com

[25] J. Zhao, X. Yang, Y. Huang, F. Du, Y. Zeng, *ACS Appl. Mater. Interfaces* **2021**, *13*, 58674.

[26] J. Dąbrowa, M. Stygar, A. Mikuła, A. Knapik, K. Mroczka, W. Tejchman, M. Danielewski, M. Martin, *Mater. Lett.* **2018**, *216*, 32.

[27] H. Chen, N. Qiu, B. Wu, Z. Yang, S. Sun, Y. Wang, *RSC Adv.* **2020**, *10*, 9736.

[28] J. Wang, Y. Cui, Q. Wang, K. Wang, X. Huang, D. Stenzel, A. Sarkar, R. Azmi, T. Bergfeldt, S. S. Bhattacharya, R. Kruk, H. Hahn, S. Schweidler, T. Brezesinski, B. Breitung, *Sci. Rep.* **2020**, *10*, 18430.

[29] Z. Teng, L. Zhu, Y. Tan, S. Zeng, Y. Xia, Y. Wang, H. Zhang, *J. Eur. Ceram. Soc.* **2020**, *40*, 1639.

[30] V. M. Goldschmidt, *Naturwissenschaften* **1926**, *14*, 477.

[31] L. H. Ahrens, *Geochim. Cosmochim. Acta* **1952**, *2*, 155.

[32] R. D. Shannon, *Acta. Crystallogr., Sect. A: Found. Adv.* **1976**, *32*, 751.

[33] B. Liu, L. Li, X. Q. Liu, X. M. Chen, *J. Mater. Chem. C* **2016**, *4*, 4684.

[34] B. M. Liu, W. J. Gan, S. Q. Lou, R. Zou, Q. Tang, C. X. Wang, J. Jiao, J. Wang, *J. Appl. Phys.* **2021**, *129*, 120901.

[35] H. Kojitani, K. Nishimura, A. Kubo, M. Sakashita, K. Aoki, M. Akaogi, *Phys. Chem. Miner.* **2003**, *30*, 409.

[36] P. McMillan, N. Ross, *Phys. Chem. Miner.* **1988**, *16*, 21.

[37] A. Sarkar, C. Loho, L. Velasco, T. Thomas, S. S. Bhattacharya, H. Hahn, R. Djenadic, *Dalton Trans.* **2017**, *46*, 12167.

[38] M. Alaydrus, M. Sakaue, N. H. Linh, S. M. Aspera, T. D. K. Wungu, H. Kasai, *ECS Trans.* **2015**, *68*, 369.

[39] J. J. Kim, S. R. Bishop, D. Chen, H. L. Tuller, *Chem. Mater.* **2017**, *29*, 1999.

[40] G. R. Remya, S. Solomon, J. K. Thomas, A. John, *AIP Conf. Proc.* **2015**, *1576*, 102.

[41] G. R. Remya, S. Solomon, J. K. Thomas, A. John, *Mater. Today Proc.* **2015**, *2*, 1012.

[42] Sandeep, D. P. Rai, A. Shankar, M. P. Ghimire, A. P. Sakhya, T. P. Sinha, R. Khenata, S. B. Omran, R. K. Thapa, *Chin. Phys. B* **2016**, *25*, 067101.

[43] B. B. de Oliveira Neto, C. da Costa Pinto, L. da Silva Marques, P. Chaudhuri, A. Ghosh, D. M. Trichês, S. M. de Souza, *J. Solid State Chem.* **2021**, *298*, 122097.

[44] M. Szubka, E. Talik, A. Molak, S. Turczyński, D. A. Pawlak, *Cryst. Res. Technol.* **2010**, *45*, 1309.

[45] K. Michel, T. S. Bjørheim, T. Norby, J. Janek, M. T. Elm, *J. Phys. Chem. C* **2020**, *124*, 15831.

[46] J. J. Kim, S. R. Bishop, N. J. Thompson, D. Chen, H. L. Tuller, *Chem. Mater.* **2014**, *26*, 1374.

[47] J. J. Kim, S. R. Bishop, N. Thompson, Y. Kuru, H. L. Tuller, *Solid State Ionics* **2012**, *225*, 198.

[48] B. E. McNealy, J. L. Hertz, *Solid State Ionics* **2014**, *256*, 52.

[49] J. Fleig, *Solid State Ionics* **2002**, *150*, 181.

[50] T. Basyuk, L. Vasylechko, I. Syvorotka, U. Schmidt, D. Trots, R. Niewa, *Phys. Status Solidi C* **2009**, *6*, 1008.

[51] A. Yoshikawa, A. Saitow, H. Horiuchi, T. Shishido, T. Fukuda, *J. Alloys Compd.* **1998**, *266*, 104.

[52] T. Ishihara, H. Furutani, H. Arikawa, M. Honda, T. Akbay, Y. Takita, *J. Electrochem. Soc.* **1999**, *146*, 1643.

[53] D. R. Ou, T. Mori, F. Ye, T. Kobayashi, J. Zou, G. Auchterlonie, J. Drennan, *Appl. Phys. Lett.* **2006**, *89*, 171911.

[54] M. T. Elm, J. D. Hofmann, C. Suchomski, J. Janek, T. Brezesinski, *ACS Appl. Mater. Interfaces* **2015**, *7*, 11792.

[55] M. Filal, C. Petot, M. Mokchah, C. Chateau, J. L. Carpentier, *Solid State Ionics* **1995**, *80*, 27.

[56] J. Koettgen, S. Grieshammer, P. Hein, B. O. H. Grope, M. Nakayama, M. Martin, *Phys. Chem. Chem. Phys.* **2018**, *20*, 14291.

[57] J. Y. Park, G. M. Choi, *Solid State Ionics* **2002**, *154–155*, 535.

[58] T. Ishihara, H. Matsuda, Y. Takita, *J. Electrochem. Soc.* **1994**, *141*, 3444.

[59] K. Michel, J. P. Eufinger, G. Ulbrich, M. Lerch, J. Janek, M. T. Elm, *Phys. Chem. Chem. Phys.* **2017**, *19*, 17661.

[60] H. L. Tuller, S. R. Bishop, D. Chen, Y. Kuru, J. J. Kim, T. S. Stefanik, *Solid State Ionics* **2012**, *225*, 194.

[61] A. Sarkar, B. Eggert, L. Velasco, X. Mu, J. Lill, K. Ollefs, S. S. Bhattacharya, H. Wende, R. Kruk, R. A. Brand, H. Hahn, *APL Mater.* **2020**, *8*, 051111.

[62] J. A. Fortner, E. C. Buck, *Appl. Phys. Lett.* **1996**, *68*, 3817.

[63] H. L. Tuller, A. S. Nowick, *J. Phys. Chem. Solids* **1977**, *38*, 859.

[64] R. F. Egerton, K. Wong, *Ultramicroscopy* **1995**, *59*, 169.

[65] X. Guo, W. Sigle, J. Maier, *J. Am. Ceram. Soc.* **2003**, *86*, 77.

[66] X. Guo, R. Waser, *Solid State Ionics* **2004**, *173*, 63.

[67] E. Celik, Y. Ma, T. Brezesinski, M. T. Elm, *Phys. Chem. Chem. Phys.* **2021**, *23*, 10706.

[68] K. L. Duncan, Y. Wang, S. R. Bishop, F. Ebrahimi, E. D. Wachsman, *J. Appl. Phys.* **2007**, *101*, 31.

[69] J. D. Solier, I. Cachadina, A. Dominguez-Rodriguez, *Phys. Rev. B* **1993**, *48*, 3704.

[70] S. Kim, M. C. Chun, K. T. Lee, H. L. Lee, *J. Power Sources* **2001**, *93*, 279.

[71] P. S. Manning, J. D. Sirman, R. A. De Souza, J. A. Kilner, *Solid State Ionics* **1997**, *100*, 1.

[72] C. Ahamer, A. K. Opitz, G. M. Rupp, J. Fleig, *J. Electrochem. Soc.* **2017**, *164*, F790.

[73] H. Hayashi, H. Inaba, M. Matsuyama, N. G. Lan, M. Dokiya, H. Tagawa, *Solid State Ionics* **1999**, *122*, 1.

[74] P. Huang, A. Petric, *J. Electrochem. Soc.* **1996**, *143*, 1644.